NANO LETTERS

pubs.acs.org/NanoLett

Letter

Superconducting Sr_2RuO_4 Thin Films without Out-of-Phase Boundaries by Higher-Order Ruddlesden–Popper Intergrowth

Jinkwon Kim,[●] Junsik Mun,[●] Carla M. Palomares García, Bongju Kim, Robin S. Perry, Yongcheol Jo, Hyunsik Im, Han Gyeol Lee, Eun Kyo Ko, Seo Hyoung Chang, Suk Bum Chung, Miyoung Kim, Jason W. A. Robinson, Shingo Yonezawa, Yoshiteru Maeno, Lingfei Wang,* and Tae Won Noh*

Cite This: *Nano Lett.* 2021, 21, 4185–4192

Read Online

ACCESS | Metrics & More | Article Recommendations | Supporting Information

ABSTRACT: Ruddlesden–Popper (RP) phases ($A_{n+1}B_nO_{3n+1}$, n = 1, 2,···) have attracted intensive research with diverse functionalities for device applications. However, the realization of a high-quality RP-phase film is hindered by the formation of out-of-phase boundaries (OPBs) that occur at terrace edges, originating from lattice mismatch in the c-axis direction with the $A'B'O_3$ ($n = \infty$) substrate. Here, using strontium ruthenate RP-phase Sr_2RuO_4 (n = 1) as a model system, an experimental approach for suppressing OPBs was developed. By tuning the growth parameters, the $Sr_3Ru_2O_7$ (n = 2) phase was formed in a controlled manner near the film–substrate interface. This higher-order RP-phase then blocked the subsequent formation of OPBs, resulting in nearly defect-free Sr_2RuO_4 layer at the upper region of the film. Consequently, the Sr_2RuO_4 thin films exhibited superconductivity up to 1.15 K, which is the highest among Sr_2RuO_4 films grown by pulsed laser deposition. This work paves the way for synthesizing pristine RP-phase heterostructures and exploring their unique physical properties.

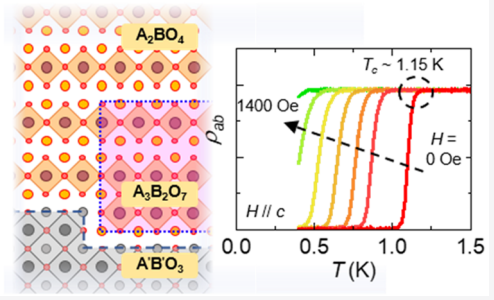

KEYWORDS: *Ruddlesden–Popper phase, out-of-phase boundary, Sr_2RuO_4 thin films, unconventional superconductivity, pulsed laser deposition*

The layered Ruddlesden–Popper (RP) phase ($A_{n+1}B_nO_{3n+1}$, n = 1, 2,···) is a homologous series of perovskite structures,[1] consisting of n layers of ABO_3 perovskite and an AO rock-salt monolayer stacked in an alternating order along the c-axis direction. Compared to conventional ABO_3 ($n = \infty$) perovskite oxides, the RP-phase offers an additional degree of freedom to tune dimensionality and thus stimulate a variety of intriguing physical phenomena and superior functionalities. Examples include the spin–orbital-coupled J_{eff} = 1/2 Mott state,[2] hybrid improper ferroelectricity,[3] anisotropic colossal magnetoresistance,[4] and significantly suppressed dielectric loss.[5] These emergent phenomena and functionalities are expected to provide a basis for novel oxide-based electronic and spintronic device applications.[6]

In comparison to simple ABO_3 perovskites, synthesizing the pure RP-phase in single-crystal form is more challenging. RP-phases with the same elements and unequal n usually have a similar thermodynamic energy landscape; during the growth of RP-phase crystals, homologous RP structures can easily lead to intergrowth.[7,8] These obstacles can be overcome by epitaxially growing the RP-phase thin films on $A'B'O_3$ perovskite substrates. Structural constraints from the substrate and precisely monitored growth conditions can effectively suppress secondary phases and stacking faults, thus facilitating a single-crystalline RP structure.[8−10] However, the difference in lattice structure between the RP-phase film and ABO_3 perovskite substrate inevitably induces another spatially extended structural defect, so-called out-of-phase boundaries (OPBs).[11]

OPBs are translational boundaries between adjacent crystal regions that are misaligned by a fraction of a unit-cell parameter.[8] As depicted schematically in Figure 1a, when A_2BO_4 (n = 1 RP-phase) thin films are grown on $A'B'O_3$ (001) substrates, the one-unit-cell-high terrace edge of the substrate causes a fractional translation of the A_2BO_4 lattice along the c-axis. This lattice translation cannot be accommodated in the A_2BO_4 film because its c-lattice constant (12–13 Å) and half of the lattice parameter (6–6.5 Å) are distinct from that of the $A'B'O_3$ substrate (~4 Å). Consequently, an array of dislocations nucleates at the terrace edge and propagates through the entire RP-phase film, forming the OPB. Given that a terrace structure is inevitable in atomically flat perovskite substrate surfaces due to the vicinal cut of the substrate, the

Received: December 17, 2020
Revised: April 29, 2021
Published: May 12, 2021

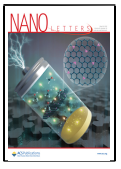

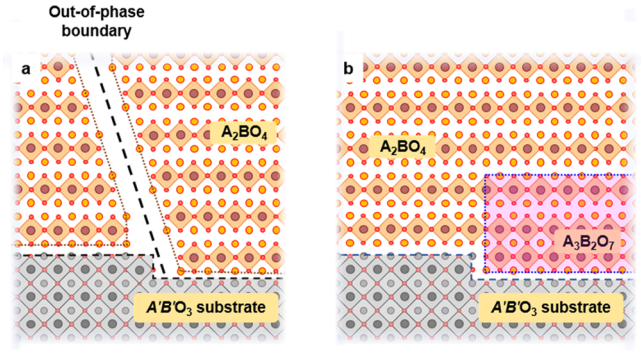

Figure 1. Schematic illustrations of Ruddlesden–Popper (RP) oxide films grown on $A'B'O_3$ (001) perovskite substrates. (a) Single-phase A_2BO_4. At the substrate terrace edges, the lattice translation along the *c*-axis can induce an array of dislocations along the A_2BO_4 [101] direction, named out-of-phase boundaries (OPBs). (b) A_2BO_4 thin film with mixed $A_3B_2O_7$ phase. The $A_3B_2O_7$ intergrowth at the film–substrate interface can compensate for the lattice translation at the terrace edges and thus suppress OPB formation.

formation of OPBs is widely observed in RP-phase epitaxial thin film growth.[8]

As an unavoidable modulation of the film structure, the OPB has a significant impact on the physical properties of RP-phase epitaxial films.[12−18] The most representative example is superconductivity in Sr_2RuO_4 (SRO214) thin films. The superconducting critical temperature (T_c) of a bulk SRO214 single crystal is around 1.5 K.[19,20] Despite the relatively low T_c, SRO214 has been studied intensively and might be a topological superconductor with potential application in quantum computing.[20−22] Recently, the debate over the nature of the superconducting symmetry of SRO214 has intensified,[23,24] and new experimental approaches are required to clarify the underlying physics of this material.[25−28] High-quality SRO214 thin films with robust superconductivity could lead to the development of Josephson junctions or spin-valve devices with a well-controlled geometry, which is important for detailed studies of the superconducting state.[29,30] However, superconducting SRO214 thin film growth is challenging owing to the unconventional nature of the pairing symmetry and the long in-plane superconducting coherence length ($\xi_{ab} \sim$ 66 nm).[31,32] In particular, structural defects are considered to be detrimental to the superconductivity of SRO214.[33] SRO214 thin films are usually grown on perovskite-structured $NdGaO_3$ or $(LaAlO_3)_{0.3}(Sr_2AlTaO_6)_{0.7}$ (LSAT) substrates in which high-density OPBs or mosaic tilts easily form.[34−36] The presence of such planar defects easily destroys the superconductivity,[12,13,34,36] and so, achieving reproducible superconductivity in SRO214 thin films remains challenging.[34−37]

Here, using SRO214 thin films as a model system we designed an experimental approach to suppress OPBs in RP-phase films by pulsed laser deposition (PLD). We intentionally induced a higher-order RP-phase (e.g., the $A_3B_2O_7$ phase) near the interface between the A_2BO_4 films and $A'B'O_3$ substrate, as depicted schematically in Figure 1b. These higher-order RP stacking faults compensate for the unfavorable lattice translation near the terrace edge, thus suppressing the formation of OPBs. Using this method, we obtained single-crystalline and nearly defect-free SRO214 layers at the upper region of the film. Consequently, the SRO214 thin films exhibited robust superconductivity with a sharp resistive transition ($\Delta T_c \sim 0.1$ K). We observed an optimized onset T_c of up to 1.15 K, which is the highest value reported among homogeneous SRO214 thin films grown by PLD. Our work provides an approach to overcoming the formation of OPBs in RP-phase films, thus facilitating exploitation of the intriguing properties of the RP-phase oxides and development of RP-phase-based functional devices.

Epitaxial SRO214 thin films were grown on (001)-oriented LSAT substrates by PLD. We investigated how the substrate temperature (T_{sub}) affected the thermodynamic equilibrium of the strontium ruthenate RP-phase (Figure S1 in the Supporting Information), when other growth parameters (oxygen partial pressure, laser fluence, and laser repetition rate) were kept constant (see Methods in the Supporting Information). At T_{sub} = 840 and 860 °C, the film structure exhibited mixed SRO214 and $Sr_3Ru_2O_7$ (SRO327) phases, while T_{sub} = 880 and 900 °C gave SRO214 single phase with epitaxial structure. On the basis of the phase modulation of strontium ruthenate films according to the change in T_{sub}, we employed two sets of growth parameters at different T_{sub} values for deposition. For Condition A, we maintained T_{sub} = 880 °C over the entire deposition period (Figure 2a, left panel). For Condition B, we gradually increased T_{sub} from 840 to 880 °C during deposition (Figure 2a, right panel).

Growth Conditions A and B produced distinct structural characteristics in the SRO214 thin films. Figure 2b,c shows X-ray diffraction (XRD) ω-2θ scans of the two SRO214 thin films grown under Conditions A and B (denoted as Samples

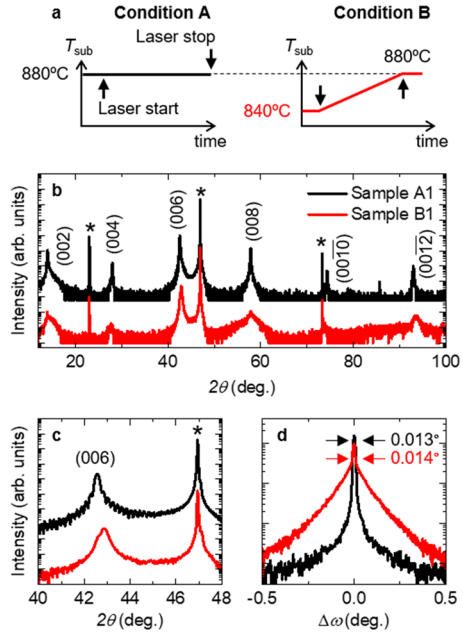

Figure 2. Structural characterizations of SRO214 thin films grown under two conditions. (a) T_{sub} for growth Conditions A and B. For growth Condition A, we maintained T_{sub} at 880 °C for the entire growth period. For growth Condition B, we gradually increased T_{sub} from 840 to 880 °C. (b) X-ray diffraction ω-2θ scans for SRO214 films grown under Conditions A and B (denoted as Samples A1 and B1, respectively). Diffractions from SRO214 are labeled as (00*l*) and diffractions from the $(LaAlO_3)_{0.3}(Sr_2AlTaO_6)_{0.7}$ (LSAT) substrate are indicated by asterisks. (c) ω-2θ scans of SRO214 (006) diffraction. The SRO214 (006) peak from Sample A1 shows clear Kiessig fringes, whereas the peak from Sample B1 becomes asymmetric. (d) Rocking curves of SRO214 (006) diffraction for Samples A1 and B1. The full width at half-maximum values are provided.

https://doi.org/10.1021/acs.nanolett.0c04963
Nano Lett. 2021, 21, 4185−4192

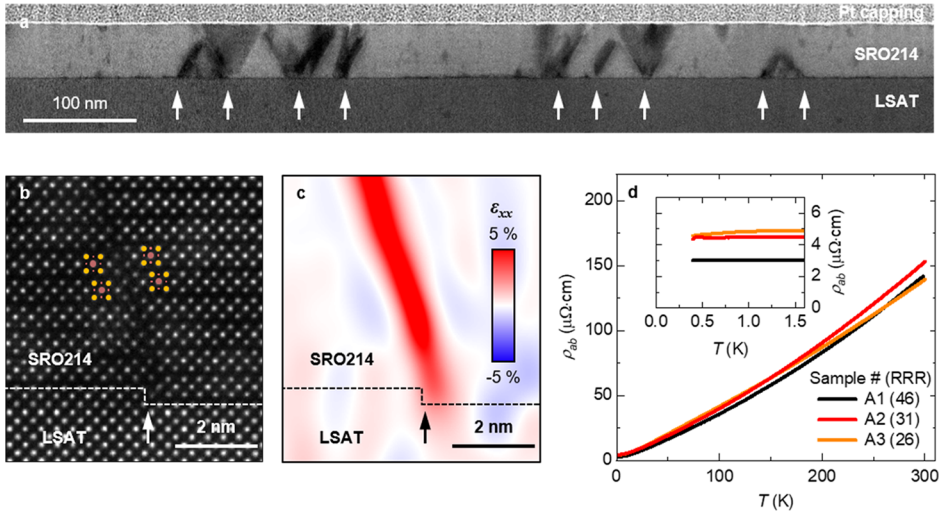

Figure 3. Microscopic structure and electrical transport of Sample A1. (a) Large-scale annular bright field-scanning transmission electron microscopy (ABF-STEM) image of Sample A1. The OPBs are indicated by white arrows. (b) An enlarged high-angle annular dark-field STEM (HAADF-STEM) image near a representative OPB. The film−substrate interface is indicated by the dashed line. As indicated by the white arrow, the OPB formed near the terrace edge. The zone axes for all images are [100]. (c) In-plane strain (ε_{xx}) map, derived from (b) by geometrical phase analysis (GPA). The layered structure of the SRO214 thin film is disconnected at the OPB. (d) Temperature-dependent in-plane resistivity [$\rho_{ab}(T)$] curves for Sample set A. The residual resistivity ratio (RRR) values of these samples are provided.

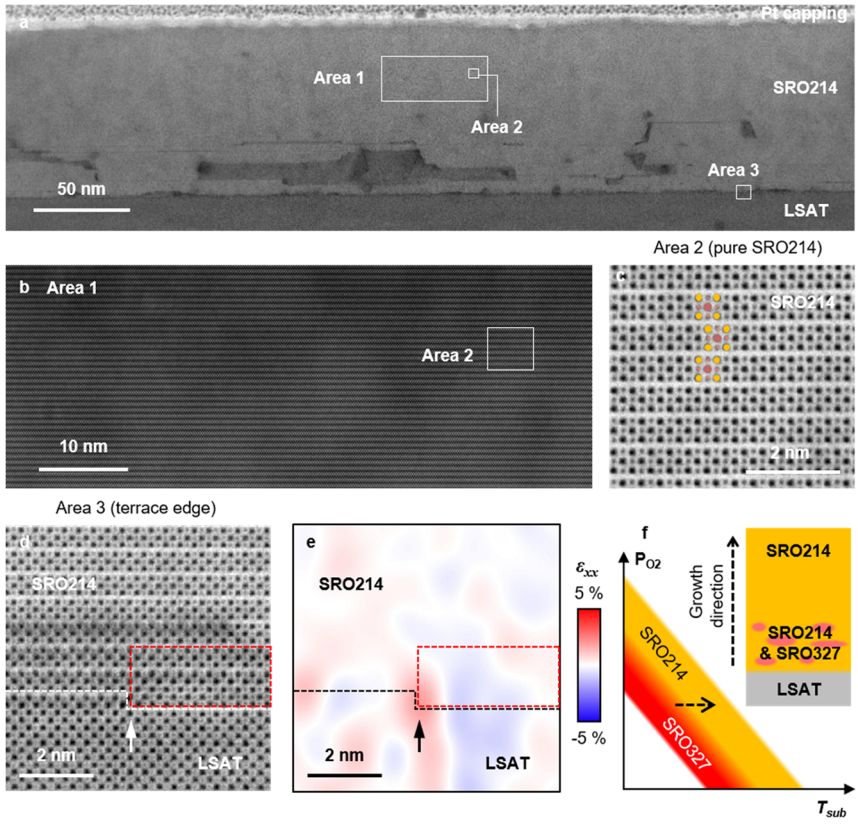

Figure 4. Microscopic structure of Sample B1. (a) Large scale ABF-STEM image of Sample B1. The image does not show any signs of OPBs. However, numerous darker and cloudlike areas of contrast appear near the film−substrate interface. (b) An enlarged HAADF-STEM image of Area 1 (indicated by the solid box in (a)). (c) Atomically resolved ABF-STEM image of Area 2 (indicated by the solid boxes in (a,b)). The ABF-STEM images in (b,c) indicate that the upper region of Sample B1 is composed of a nearly defect-free SRO214 layer. (d) Atomically resolved ABF-STEM image measured from Area 3 (indicated by the solid box in (a)). The film−substrate interface is indicated by the dashed line. A half-unit cell of SRO327 phase accommodates the step-height of the substrate (indicated by a red box). The zone axes for all images are [100]. (e) ε_{xx} map of Area 3 converted by GPA. (f) Schematic thermodynamic phase diagram for SRO214 growth (adapted from ref 37, licensed under a Creative Commons Attribution (CC BY) license). The lower T_{sub} facilitates the formation of mixed SRO214 and SRO327 phases. Therefore, the linearly increasing T_{sub} during film growth results in SRO327 intergrowth near the interface and pure SRO214 phase at the upper region of the films.

https://doi.org/10.1021/acs.nanolett.0c04963
Nano Lett. 2021, 21, 4185−4192

A1 and B1, respectively). For Sample A1, the wide-range ω-2θ scan (Figure 2b) shows multiple diffraction peaks perfectly indexed to the pure SRO214 phase with the (006) diffraction peak showing well-defined Kiessig fringes (Figure 2c). These results, combined with the reciprocal space mapping (RSM) and the surface topography analysis (Figure S2a,b in the Supporting Information, respectively), confirm a high-quality epitaxial and pseudomorphic structure of Sample A1. In contrast, the ω-2θ scan for Sample B1 (Figure 2b) shows broad diffraction peaks compared to Sample A1. The (006) diffraction peak (Figure 2c), RSM and surface topography (Figure S2c,d in the Supporting Information, respectively) exhibited an asymmetric double-peak feature, implying a structural gradient along the *c*-axis direction, and degraded film structure. Figure 2d shows the rocking curves of the SRO214 (006) diffractions for Samples A1 and B1. Sample A1 exhibited a sharp and narrow rocking curve indicating good crystallinity having a full width at half-maximum (fwhm) value of 0.013°, which is comparable to the LSAT substrate (0.010°, Figure S2e in the Supporting Information). Sample B1 also exhibited a sharp rocking curve (fwhm ∼0.014°), but it was buried in a broad shoulder. This shoulder had a 10-fold larger fwhm value (∼0.144°) than that of Sample A1. We suggest that the broadening observed in the rocking curve of Sample B1 may be attributable to dislocations or mosaicity that disturb the epitaxial structure of Sample B1.

The microscopic structure of the SRO214 films was investigated by scanning transmission electron microscopy (STEM). We first analyzed the annular bright-field (ABF)-STEM image of Sample A1. As shown in Figure 3a, although the XRD measurements indicated a high-quality epitaxial structure, the ABF-STEM image revealed high-density OPBs (marked by white arrows).[12,13,34,36] Figure 3b shows an atomic-resolved high-angle annular dark field (HAADF)-STEM image from Figure 3a near the film−substrate interface (indicated by a dashed line). At the terrace edge of the LSAT substrate (indicated by a white arrow), the SRO214 film exhibited a lattice translation by the height of a single ABO_3 unit-cell (∼4 Å) along the *c*-axis direction.[36] As a result, an OPB emerged at the terrace edges of the substrate and extended to the film surface. The OPB was inclined by 73° from the (001) plane, corresponding to the SRO214 [101] direction.[12] Figure 3c shows an in-plane strain mapping [ε_{xx}, converted by geometrical phase analysis (GPA);[38] see Methods in the Supporting Information]. Note that the value of ε_{xx} in the OPB region was higher than 5%. This huge local lattice defect breaks the continuity of the layered structure of SRO214, resulting in suppression of the coherence of Cooper pairs. Considering that the typical distance between OPBs is comparable to the ξ_{ab} (∼66 nm) of SRO214, the superconductivity of Sample A1 should be affected by the presence of OPBs.[12,13,34,36]

To understand how OPBs affect superconductivity in SRO214 thin films, we measured the temperature-dependence of the in-plane resistivity [$\rho_{ab}(T)$] for three SRO214 thin films grown under Condition A (denoted as Samples A1−A3). As shown in Figure 3d, Samples A1−A3 exhibited low residual resistivities at 2 K [ρ_{ab}(2 K)] of 3.0, 4.6, and 4.9 $\mu\Omega$·cm, respectively, with high residual resistivity ratios [RRR = ρ_{ab}(300 K)/ρ_{ab}(2 K)] of 46, 31, and 26. The thicknesses of Samples A1−A3 were 58.0, 54.0, and 94.9 nm, respectively. Note that the ρ_{ab} of Sample set A was proportional to T^2, which is indicative of SRO214.[39,40] Nevertheless, we only observed a plateau or slight drop in ρ_{ab} down to 0.4 K (inset), indicating the absence of superconductivity or possibly incipient superconductivity, at best. Given that Sample set A exhibited no evidence of Ru deficiency according to Raman spectroscopy measurements (Figure S3 in the Supporting Information),[41] we suggest that the high-density of OPBs is responsible for the absence of superconductivity in Sample set A.

In contrast to the high-density OPBs in Sample set A, Sample B1 exhibited distinct structural defects. The ABF-STEM image of Sample B1 did not show OPB-like contrast or mosaic tilt (Figure 4a). Instead, the image exhibited a nearly defect-free region at the upper region of the film. The enlarged HAADF- and ABF-STEM images (Figure 4b,c, respectively) confirm that the region labeled as Areas 1 and 2 was nearly a perfect single-crystalline SRO214 layer. This high-quality SRO214 region spanned over 500 nm, which is 1 order of magnitude larger than ξ_{ab}. In addition, Figure 4a shows numerous dark-patches near the interface region. These patches were shown to be the SRO327 phase on atomic-resolution ABF-STEM images (Figure S4 in the Supporting Information). Figure 4d shows the atomic-resolution ABF-STEM image of Area 3, at the film−substrate interface of Sample B1. A half-unit cell of SRO327 phase formed at the down step region of the terrace edge (indicated by the red box), while the SRO214 phase was grown on the upper step region. The SRO327 phase accommodated the step-height of the LSAT substrate (∼4 Å). Above the SRO327 phase, smooth boundaries were formed and defect-free SRO214 layers could be grown through the whole region, as depicted schematically in Figure 1b. Figure 4e shows an ε_{xx} map of Area 3, converted by GPA. At the terrace edge, tensile strain (red-colored) was observed, similar to the Sample A1 (Figure 3c). However, the huge tensile strain propagation did not occur in Sample B1 due to the accommodation of the step-height by the SRO327 phase. Hence, the accumulated SRO327 phase at the film−substrate interface plays a crucial role in the suppression of OPB formation. The SRO327 intergrowth observed in the STEM images was consistent with the XRD results shown in Figure 2. The disarranged stacking sequence derived from SRO327 intergrowth created a structural gradient in Sample set B, inducing asymmetric and double-peak features of (006) diffraction in the ω-2θ scan and a diffusive background in the rocking curve. The defect-free SRO214 layers contributed to the sharp peak in the rocking curve.

We now consider the origin of SRO327 intergrowth in Condition B. The thermodynamic phase diagram of the strontium ruthenate RP-phase is plotted schematically in Figure 4f. For Condition B, we initiated the deposition at a relatively low T_{sub} of 840 °C, which may have facilitated the formation of a mixed SRO214 and SRO327 phase. As T_{sub} increased, the pure SRO214 phase became more energetically favorable (Figure S1 in the Supporting Information). Hence, the gradual increase in T_{sub} during deposition could promote the formation of a pure SRO214 phase at the upper region of the film. The self-organized SRO327 phases interrupted the periodic arrangement of layered structure, breaking the continuous propagation of OPBs and allowing to the growth of defect-free SRO214 layers above the intergrowth layer.

The defect-free SRO214 layers led to robust superconductivity. Figure 5a shows $\rho_{ab}(T)$ curves of Sample set B (denoted as Samples B1−B7). As shown in Figure 5a,b, Sample set B exhibited ρ_{ab}(2 K) from 2.3 to 6.7 $\mu\Omega$·cm with

https://doi.org/10.1021/acs.nanolett.0c04963
Nano Lett. 2021, 21, 4185−4192

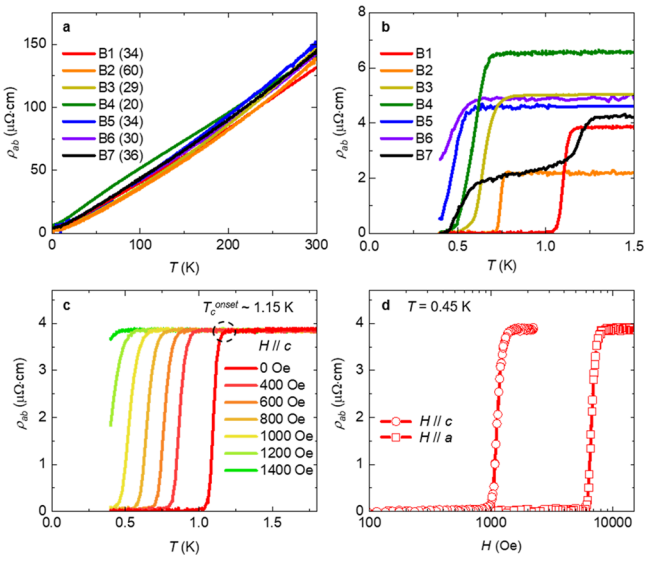

Figure 5. Electrical transport of Sample set B. (a) $\rho_{ab}(T)$ curve measured from Sample set B. The RRR values of these samples are provided. (b) $\rho_{ab}(T)$ curves of Sample set B in the low-T range. All seven samples show superconducting transitions. The onset superconducting transition temperature (T_c) varies from 0.50 to 1.30 K. (c) $\rho_{ab}(T)$ curves in the low-T range measured for Sample B1 obtained under various magnetic fields (H). The fields were applied along the c-axis. The onset T_c at zero-field (indicated by a dashed circle) is 1.15 K. (d) $\rho_{ab}(H)$ curves of Sample B1 with H applied along the c- and a-axis directions.

RRR values from 21 to 60. The thickness varied from 87.2 to 140.6 nm. In the low-T range, all of Sample set B showed superconducting transitions (Figure 5b). The highest onset T_c was 1.30 K (Sample B7), which is the highest value reported among the superconducting SRO214 thin films. Despite the notable T_c, the broad superconducting transition indicated percolative superconductivity of Sample B7. To explore the superconductivity of Sample set B further, we systematically characterized the superconductivity of Sample B1. At zero magnetic field, Sample B1 exhibited superconductivity up to 1.15 K, which represents the highest onset T_c among reported homogeneous PLD-grown thin films,[34,35] comparable to molecular beam epitaxy-grown thin films.[36] Moreover, the superconducting transition width was within $\Delta T_c \sim 0.1$ K, which is the sharpest transition reported among epitaxial SRO214 thin films and is close to the value for the high-quality single crystals.[42] These findings indicate homogeneous superconductivity throughout the SRO214 thin films. Figure 5c shows the $\rho_{ab}(T)$ curves of Sample B1 under various external magnetic fields (H) in the c-axis direction. The superconducting transition of Sample B1 shifted gradually with increasing H. Figure 5d shows the $\rho_{ab}(H)$ curves of Sample B1 at $T = 0.45$ K. The upper critical fields (H_{c2}) are 0.15 and 0.80 T for H applied in the c- and a-axis directions, respectively. Note that these H_{c2} values are different from the bulk values of 0.08 and 1.50 T along the c- and a-axis directions, respectively.[31] Such substantial changes in H_{c2} can be explained by the dimensional crossover in the thin films which can induce **d**-vector flipping parallel to the in-plane direction,[43] or a small field misalignment during the measurement of in-plane H_{c2} could be attributed.

We now discuss the variation in the T_c within Sample set B (from 0.50 to 1.30 K; Figure 5b). The thickness of the defect-free SRO214 layers (t_{214}) was positively correlated with superconductivity (Figure S5 in the Supporting Information). This tendency can be understood as thickness-dependent superconductivity, which is generally observed in superconducting thin films.[44,45] As the film becomes thinner, the reduced dimension and increased disorder usually degrade the superconductivity. We speculate that the t_{214} varies from sample to sample, resulting in the observed variations in electrical transport and superconductivity. During the deposition of Sample set B, the microstructure may not be precisely controlled by T_{sub} engineering due to the similarities in Gibbs formation energies between SRO214 and SRO327 phases.[7] In addition, the high kinetic energy scale of PLD (~100 eV) provides a dynamic environment in which the intergrowth can be randomly formed during deposition. Despite the difficulties in control, the presence of the SRO327 phase ensures the Ru-rich environment as well as suppression of OPBs, which are both essential for superconductivity in SRO214 thin films. Note that the SRO327 intergrowth at the film–substrate interface was also reported previously for superconducting SRO214 thin films.[35,37] Therefore, we suggest that SRO327 intergrowth engineering could be effective for achieving superconductivity in SRO214 films, and our thermodynamic method could promote the comprehensive realization of superconducting SRO214 films. Identifying experimental approaches for improved control over SRO327 intergrowth should be a target for future investigations.

In conclusion, we have successfully grown superconducting SRO214 films by inducing SRO327 intergrowth near the film–substrate interface. The intergrowth was controlled by T_{sub} during growth and interface–intergrowth formation blocks lattice translation at the terrace edges of the substrate, thus suppressing OPB formation. The nearly defect-free SRO214 layers were formed above the intergrowth layers and facilitated homogeneous superconductivity with a transition temperature of 1.15 K and a sharp superconducting transition width of 0.1 K. A synthesis approach to inhibit OPB formation is key for the development of versatile RP-phase-based oxide heterostructures and creates opportunities for the development of novel functional devices.

■ ASSOCIATED CONTENT

Supporting Information

The Supporting Information is available free of charge at https://pubs.acs.org/doi/10.1021/acs.nanolett.0c04963.

Additional characterization data, and spectroscopy data are included (PDF)

■ AUTHOR INFORMATION

Corresponding Authors

Lingfei Wang − *Hefei National Laboratory for Physical Sciences at Microscale, University of Science and Technology of China, Hefei 230026, China; Center for Correlated Electron Systems, Institute for Basic Science (IBS), Seoul 08826, Republic of Korea; Department of Physics and Astronomy, Seoul National University, Seoul 08826, Republic of Korea;* orcid.org/0000-0003-1675-0941; Email: wanglf@ustc.edu.cn

Tae Won Noh − *Center for Correlated Electron Systems, Institute for Basic Science (IBS), Seoul 08826, Republic of Korea; Department of Physics and Astronomy, Seoul National University, Seoul 08826, Republic of Korea;*

https://doi.org/10.1021/acs.nanolett.0c04963
Nano Lett. 2021, 21, 4185−4192

orcid.org/0000-0003-1905-2321; Email: twnoh@snu.ac.kr

Authors

Jinkwon Kim − *Center for Correlated Electron Systems, Institute for Basic Science (IBS), Seoul 08826, Republic of Korea; Department of Physics and Astronomy, Seoul National University, Seoul 08826, Republic of Korea*

Junsik Mun − *Center for Correlated Electron Systems, Institute for Basic Science (IBS), Seoul 08826, Republic of Korea; Department of Materials Science and Engineering and Research Institute of Advanced Materials, Seoul National University, Seoul 08826, Republic of Korea*

Carla M. Palomares García − *Department of Materials Science & Metallurgy, University of Cambridge, Cambridge CB3 0FS, United Kingdom*

Bongju Kim − *Center for Correlated Electron Systems, Institute for Basic Science (IBS), Seoul 08826, Republic of Korea; Department of Physics and Astronomy, Seoul National University, Seoul 08826, Republic of Korea*

Robin S. Perry − *London Centre for Nanotechnology and UCL Centre for Materials Discovery, University College London, London WC1E 6BT, United Kingdom; ISIS Facility, Rutherford Appleton Laboratory, Chilton, Didcot OX11 0QX, United Kingdom; Department of Physics, Kyoto University, Kyoto 606-8502, Japan*

Yongcheol Jo − *Quantum Functional Semiconductor Research Center (QSRC), Dongguk University, Seoul 04620, Republic of Korea*

Hyunsik Im − *Division of Physics and Semiconductor Science, Dongguk University, Seoul 04620, Republic of Korea*

Han Gyeol Lee − *Center for Correlated Electron Systems, Institute for Basic Science (IBS), Seoul 08826, Republic of Korea; Department of Physics and Astronomy, Seoul National University, Seoul 08826, Republic of Korea*

Eun Kyo Ko − *Center for Correlated Electron Systems, Institute for Basic Science (IBS), Seoul 08826, Republic of Korea; Department of Physics and Astronomy, Seoul National University, Seoul 08826, Republic of Korea*

Seo Hyoung Chang − *Department of Physics, Chung-Ang University, Seoul 06974, Republic of Korea;* orcid.org/0000-0002-1012-7983

Suk Bum Chung − *Department of Physics and Natural Science Research Institute, University of Seoul, Seoul 02504, Republic of Korea; School of Physics, Korea Institute for Advanced Study, Seoul 02455, Republic of Korea*

Miyoung Kim − *Center for Correlated Electron Systems, Institute for Basic Science (IBS), Seoul 08826, Republic of Korea; Department of Materials Science and Engineering and Research Institute of Advanced Materials, Seoul National University, Seoul 08826, Republic of Korea;* orcid.org/0000-0001-8632-6711

Jason W. A. Robinson − *Department of Materials Science & Metallurgy, University of Cambridge, Cambridge CB3 0FS, United Kingdom*

Shingo Yonezawa − *Department of Physics, Kyoto University, Kyoto 606-8502, Japan*

Yoshiteru Maeno − *Department of Physics, Kyoto University, Kyoto 606-8502, Japan*

Complete contact information is available at: https://pubs.acs.org/10.1021/acs.nanolett.0c04963

Author Contributions

●J.K. and J.M. contributed equally to this work.

Author Contributions

The manuscript was written through contributions of all authors. All authors have given approval to the final version of the manuscript.

Notes

The authors declare no competing financial interest.

■ ACKNOWLEDGMENTS

This work was supported by the Research Center Program of IBS (Institute for Basic Science) in Korea (IBS-R009-D1), National Research Foundation of Korea (NRF) grant funded by the Korea government (MSIT) (NRF-2017R1A2B3011629), the National Key Basic Research Program of China (Grant 2020YFA0309100), the National Natural Science Foundation of China (Grant 12074365), the Fundamental Research Funds for the Central Universities (WK2030000035, WK2340000102), EPSRC-JSPS Core-to-Core International Network "Oxide Superspin" (Nos. EP/P026311/1 and JPJSCCA20170002), JSPS KAKENHI Nos. JP15H05852, JP15K21717, and JP17H06136 funded by Japan Society for Promotion of Science (JSPS), and the Basic Science Research Program through the National Research Foundation of Korea (NRF) funded by the Ministry of Education (2016R1A6A1A03012877, 2020R1A2C1007554, and 2018R1A6A1A06024977). Experiments at PLS-II 3A beamline were supported in part by MSIT and POSTECH. STEM measurement was supported by the National Center for Inter-Universitiy Research Facilities (NCIRF) at Seoul National University in Korea. The authors acknowledge Prof. Tae Heon Kim, Dr. Gideok Kim, Dr. Yeong Jae Shin, Dr. Atsutoshi Ikeda, Dr. Mi Kyung Kim, Nahyun Lee, Jeong Rae Kim, Suhan Son, Han Gyeol Park, and Takuto Miyoshi for the technical support and fruitful discussions.

■ REFERENCES

(1) Ruddlesden, S. N.; Popper, P. New Compounds of the K_2NiF_4 Type. *Acta Crystallogr.* **1957**, *10*, 538−539.

(2) Kim, B. J.; Jin, H.; Moon, S. J.; Kim, J.-Y.; Park, B.-G.; Leem, C. S.; Yu, J.; Noh, T. W.; Kim, C.; Oh, S.-J.; Park, J.-H.; Durairaj, V.; Cao, G.; Rotenberg, E. Novel J_{eff} = 1/2 Mott State Induced by Relativistic Spin-Orbit Coupling in Sr_2IrO_4. *Phys. Rev. Lett.* **2008**, *101*, 076402.

(3) Oh, Y. S.; Luo, X.; Huang, F.-T.; Wang, Y.; Cheong, S.-W. Experimental Demonstration of Hybrid Improper Ferroelectricity and the Presence of Abundant Charged Walls in $(Ca,Sr)_3Ti_2O_7$ Crystals. *Nat. Mater.* **2015**, *14*, 407−413.

(4) Moritomo, Y.; Asamitsu, A.; Kuwahara, H.; Tokura, Y. Giant Magnetoresistance of Manganese Oxides with a Layered Perovskite Structure. *Nature* **1996**, *380*, 141−144.

(5) Lee, C.-H.; Orloff, N. D.; Birol, T.; Zhu, Y.; Goian, V.; Rocas, E.; Haislmaier, R.; Vlahos, E.; Mundy, J. A.; Kourkoutis, L. F.; Nie, Y.; Biegalski, M. D.; Zhang, J.; Bernhagen, M.; Benedek, N. A.; Kim, Y.; Brock, J. D.; Uecker, R.; Xi, X. X.; Gopalan, V.; Nuzhnyy, D.; Kamba, S.; Muller, D. A.; Takeuchi, I.; Booth, J. C.; Fennie, C. J.; Schlom, D. G. Exploiting Dimensionality and Defect Mitigation to Create Tunable Microwave Dielectrics. *Nature* **2013**, *502*, 532−536.

(6) Bibes, M.; Barthélémy, A. Oxide Spintronics. *IEEE Trans. Electron Devices* **2007**, *54*, 1003−1023.

(7) Jacob, K.T.; Thi Lwin, K.; Waseda, Y. Strontium Ruthenates: Determination of Gibbs Energies of Formation Using Electrochemical Cells. *Mater. Sci. Eng., B* **2003**, *103*, 152−161.

(8) Zurbuchen, M. A.; Tian, W.; Pan, X. Q.; Fong, D.; Streiffer, S. K.; Hawley, M. E.; Lettieri, J.; Jia, Y.; Asayama, G.; Fulk, S. J.;

Comstock, D. J.; Knapp, S.; Carim, A. H.; Schlom, D. G. Morphology, Structure, and Nucleation of Out-of-Phase Boundaries (OPBs) in Epitaxial Films of Layered Oxides. *J. Mater. Res.* **2007**, *22*, 1439−1471.
(9) Haeni, J. H.; Theis, C. D.; Schlom, D. G.; Tian, W.; Pan, X. Q.; Chang, H.; Takeuchi, I.; Xiang, X.-D. Epitaxial Growth of the First Five Members of the $Sr_{n+1}TinO_{3n+1}$ Ruddlesden−Popper Homologous Series. *Appl. Phys. Lett.* **2001**, *78*, 3292−3294.
(10) Lee, J. H.; Luo, G.; Tung, I. C.; Chang, S. H.; Luo, Z.; Malshe, M.; Gadre, M.; Bhattacharya, A.; Nakhmanson, S. M.; Eastman, J. A.; Hong, H.; Jellinek, J.; Morgan, D.; Fong, D. D.; Freeland, J. W. Dynamic Layer Rearrangement During Growth of Layered Oxide Films by Molecular Beam Epitaxy. *Nat. Mater.* **2014**, *13*, 879−883.
(11) Allpress, J. G. The Direct Observation of Structural Features and Defects in Complex Oxides by Two-Dimensional Lattice Imaging. *Mater. Res. Bull.* **1969**, *4*, 707−720.
(12) Zurbuchen, M. A.; Jia, Y.; Knapp, S.; Carim, A. H.; Schlom, D. G.; Zou, L.-N.; Liu, Y. Suppression of Superconductivity by Crystallographic Defects in Epitaxial Sr_2RuO_4 Films. *Appl. Phys. Lett.* **2001**, *78*, 2351−2353.
(13) Zurbuchen, M. A.; Jia, Y.; Knapp, S.; Carim, A. H.; Schlom, D. G.; Pan, X. Q. Defect Generation by Preferred Nucleation in Epitaxial $Sr_2RuO_4/LaAlO_3$. *Appl. Phys. Lett.* **2003**, *83*, 3891−3893.
(14) Wang, Z.; Guo, H.; Shao, S.; Saghayezhian, M.; Li, J.; Fittipaldi, R.; Vecchione, A.; Siwakoti, P.; Zhu, Y.; Zhang, J.; Plummer, E. W. Designing Antiphase Boundaries by Atomic Control of Heterointerfaces. *Proc. Natl. Acad. Sci. U. S. A.* **2018**, *115*, 9485−9490.
(15) Rijnders, G.; Curras, S.; Huijben, M.; Blank, D. H. A.; Rogalla, H. Influence of Substrate−Film Interface Engineering on the Superconducting Properties of $YBa_2Cu_3O_{7-\delta}$. *Appl. Phys. Lett.* **2004**, *84*, 1150−1152.
(16) Zurbuchen, M. A.; Asayama, G.; Schlom, D. G.; Streiffer, S. K. Ferroelectric Domain Structure of $SrBi_2Nb_2O_9$ Epitaxial Thin Films. *Phys. Rev. Lett.* **2002**, *88*, 107601.
(17) Dietl, C.; Sinha, S. K.; Christiani, G.; Khaydukov, Y.; Keller, T.; Putzky, D.; Ibrahimkutty, S.; Wochner, P.; Logvenov, G.; van Aken, P. A.; Kim, B. J.; Keimer, B. Tailoring the Electronic Properties of Ca_2RuO_4 via Epitaxial Strain. *Appl. Phys. Lett.* **2018**, *112*, 031902.
(18) Tsurumaki-Fukuchi, A.; Tsubaki, K.; Katase, T.; Kamiya, T.; Arita, M.; Takahashi, Y. Stable and Tunable Current-Induced Phase Transition in Epitaxial Thin Films of Ca_2RuO_4. *ACS Appl. Mater. Interfaces* **2020**, *12*, 28368−28374.
(19) Maeno, Y.; Hashimoto, H.; Yoshida, K.; Nishizaki, S.; Fujita, T.; Bednorz, J. G.; Lichtenberg, F. Superconductivity in a Layered Perovskite without Copper. *Nature* **1994**, *372*, 532−534.
(20) Mackenzie, A. P.; Maeno, Y. The Superconductivity of Sr_2RuO_4 and the Physics of Spin-Triplet Pairing. *Rev. Mod. Phys.* **2003**, *75*, 657−712.
(21) Ueno, Y.; Yamakage, A.; Tanaka, Y.; Sato, M. Symmetry-Protected Majorana Fermions in Topological Crystalline Superconductors: Theory and Application to Sr_2RuO_4. *Phys. Rev. Lett.* **2013**, *111*, 087002.
(22) Sarma, S. D.; Nayak, C.; Tewari, S. Proposal to Stabilize and Detect Half-Quantum Vortices in strontium Ruthenate Thin Films: Non-Abelian Braiding Statistics of Vortices in a p_x+ip_y Superconductor. *Phys. Rev. B* **2006**, *73*, 220502.
(23) Pustogow, A.; Luo, Y.; Chronister, A.; Su, Y.-S.; Sokolov, D. A.; Jerzembeck, F.; Mackenzie, A. P.; Hicks, C. W.; Kikugawa, N.; Raghu, S.; Bauer, E. D.; Brown, S. E. Constraints on the Superconducting Order Parameter in Sr_2RuO_4 from Oxygen-17 Nuclear Magnetic Resonance. *Nature* **2019**, *574*, 72−75.
(24) Ishida, K.; Manago, M.; Kinjo, K.; Maeno, Y. Reduction of the ^{17}O Knight Shift in the Superconducting State and the Heat-up Effect by NMR Pulses on Sr_2RuO_4. *J. Phys. Soc. Jpn.* **2020**, *89*, 034712.
(25) Sharma, R.; Edkins, S. D.; Wang, Z.; Kostin, A.; Sow, C.; Maeno, Y.; Mackenzie, A. P.; Davis, J. C. S.; Madhavan, V. Momentum-Resolved Superconducting Energy Gaps of Sr_2RuO_4 from Quasiparticle Interference Imaging. *Proc. Natl. Acad. Sci. U. S. A.* **2020**, *117*, 5222−5227.
(26) Benhabib, S.; Lupien, C.; Paul, I.; Berges, L.; Dion, M.; Nardone, M.; Zitouni, A.; Mao, Z. Q.; Maeno, Y.; Georges, A.; Taillefer, L.; Proust, C. Ultrasound Evidence for a Two-Component Superconducting Order Parameter in Sr_2RuO_4. *Nat. Phys.* **2021**, *17*, 194−109.
(27) Ghosh, S.; Shekhter, A.; Jerzembeck, F.; Kikugawa, N.; Sokolov, D. A.; Brando, M.; Mackenzie, A. P.; Hicks, C. W.; Ramshaw, B. J. Thermodynamic Evidence for a Two-Component Superconducting Order Parameter in Sr_2RuO_4. *Nat. Phys.* **2021**, *17*, 199−204.
(28) Grinenko, V.; Ghosh, S.; Sarkar, R.; Orain, J.-C.; Nikitin, A.; Elender, M.; Das, D.; Guguchia, Z.; Brückner, F.; Barber, M. E.; Park, J.; Kikugawa, N.; Sokolov, D. A.; Bobowski, J. S.; Miyoshi, T.; Maeno, Y.; Mackenzie, A. P.; Luetkens, H.; Hicks, C. W.; Klauss, H.-H. Split Superconducting and Time-Reversal Symmetry-Breaking Transitions in Sr_2RuO_4 Under Stress. *Nat. Phys.* **2021** DOI: 10.1038/s41567-021-01182-7.
(29) Ikegaya, S.; Yada, K.; Tanaka, Y.; Kashiwaya, S.; Asano, Y.; Manske, D. Identification of Spin-Triplet Superconductivity Through a Helical-Chiral Phase Transition in Sr_2RuO_4 Thin Films. *Phys. Rev. B: Condens. Matter Mater. Phys.* **2020**, *101*, 220501.
(30) Chung, S. B.; Kim, S. K.; Lee, K. H.; Tserkovnyak, Y. Cooper-Pair Spin Current in a Strontium Ruthenate Heterostructure. *Phys. Rev. Lett.* **2018**, *121*, 167001.
(31) Akima, T.; Nishizaki, S.; Maeno, Y. Intrinsic Superconducting Parameters of Sr_2RuO_4. *J. Phys. Soc. Jpn.* **1999**, *68*, 694−695.
(32) Mackenzie, A. P.; Haselwimmer, R. K. W.; Tyler, A. W.; Lonzarich, G. G.; Mori, Y.; Nishizaki, S.; Maeno, Y. Extremely Strong Dependence of Superconductivity on Disorder in Sr_2RuO_4. *Phys. Rev. Lett.* **1998**, *80*, 161−164.
(33) Mao, Z. Q.; Mori, Y.; Maeno, Y. Suppression of Superconductivity in Sr_2RuO_4 Caused by Defects. *Phys. Rev. B: Condens. Matter Mater. Phys.* **1999**, *60*, 610−614.
(34) Krockenberger, Y.; Uchida, M.; Takahashi, K. S.; Nakamura, M.; Kawasaki, M.; Tokura, Y. Growth of superconducting Sr_2RuO_4 thin films. *Appl. Phys. Lett.* **2010**, *97*, 082502.
(35) Palomares Garcia, C. M.; Bernardo, A. Di.; Kimbell, G.; Vickers, M. E.; Massabuau, F. C-P.; Komori, S.; Divitini, G.; Yasui, Y.; Lee, H. G.; Kim, J.; Kim, B.; Blamire, M. G.; Vecchione, A.; Fittipaldi, R.; Maeno, Y.; Noh, T. W.; Robinson, J. W. A. Pair Suppression Caused by Mosaic-Twist Defects in Superconducting Sr_2RuO_4 Thin-Films Prepared Using Pulsed Laser Deposition. *Comms. Mater.* **2020**, *1*, 23.
(36) Uchida, M.; Ide, M.; Watanabe, H.; Takahashi, K. S.; Tokura, Y.; Kawasaki, M. Molecular Beam Epitaxy Growth of Superconducting Sr_2RuO_4 Films. *APL Mater.* **2017**, *5*, 106108.
(37) Nair, H. P.; Ruf, J. P.; Schreiber, N. J.; Miao, L.; Grandon, M. L.; Baek, D. J.; Goodge, B. H.; Ruff, J. P. C.; Kourkoutis, L. F.; Shen, K. M.; Schlom, D. G. Demystifying the Growth of Superconducting Sr_2RuO_4 Thin Films. *APL Mater.* **2018**, *6*, 101108.
(38) Hÿtch, M. J.; Snoeck, E.; Kilaas, R. Quantitative Measurement of Displacement and Strain Fields from HREM Micrographs. *Ultramicroscopy* **1998**, *74*, 131−146.
(39) Maeno, Y.; Yoshida, K.; Hashimoto, H.; Nishizaki, S.; Ikeda, S.; Nohara, M.; Fujita, T.; Mackenzie, A. P.; Hussey, N. E.; Bednorz, J. G.; Lichtenberg, F. Two-Dimensional Fermi Liquid Behaviors of the Superconductor Sr_2RuO_4. *J. Phys. Soc. Jpn.* **1997**, *66*, 1405−1408.
(40) Hussey, N. E.; Mackenzie, A. P.; Cooper, J. R.; Maeno, Y.; Nishizaki, S.; Fujita, T. Normal-State Magnetoresistance of Sr_2RuO_4. *Phys. Rev. B: Condens. Matter Mater. Phys.* **1998**, *57*, 5505−5511.
(41) Kim, G.; Suyolcu, Y. E.; Herrero-Martin, J.; Putzky, D.; Nair, H. P.; Ruf, J. P.; Schreiber, N. J.; Dietl, C.; Christiani, G.; Logvenov, G.; Minola, M.; van Aken, P. A.; Shen, K. M.; Schlom, D. G.; Keimer, B. Electronic and Vibrational Signatures of Ruthenium Vacancies in Sr_2RuO_4 Thin Films. *Phys. Rev. Mater.* **2019**, *3*, 094802.
(42) Bobowski, J. S.; Kikugawa, N.; Miyoshi, T.; Suwa, H.; Xu, H.; Yonezawa, S.; Sokolov, D. A.; Mackenzie, A. P.; Maeno, Y. Improved Single-Crystal Growth of Sr_2RuO_4. *Condens. Matter* **2019**, *4*, 6.
(43) Uchida, M.; Ide, M.; Kawamura, M.; Takahashi, K. S.; Kozuka, Y.; Tokura, Y.; Kawasaki, M. Anomalous Enhancement of Upper

Critical Field in Sr_2RuO_4 Thin Films. *Phys. Rev. B: Condens. Matter Mater. Phys.* **2019**, *99*, 161111.
(44) Dubi, Y.; Meir, Y.; Avishai, Y. Nature of the Superconductor–Insulator Transition in Disordered Superconductors. *Nature* **2007**, *449*, 876–880.
(45) Ivry, Y.; Kim, C.-S.; Dane, A. E.; De Fazio, D.; McCaughan, A. N.; Sunter, K. A.; Zhao, Q.; Berggren, K. K. Universal Scaling of the Critical Temperature for Thin Films Near the Superconducting-to-Insulating Transition. *Phys. Rev. B: Condens. Matter Mater. Phys.* **2014**, *90*, 214515.

https://doi.org/10.1021/acs.nanolett.0c04963
Nano Lett. 2021, 21, 4185–4192